actuators

MDPI

Article

Development of a Sinusoidal Corrugated Dual-Axial Flexure Mechanism for Planar Nanopositioning

Yuhan Niu, Xingyou Chen, Li Chen, Zhiwei Zhu and Peng Huang *

School of Mechanical Engineering, Nanjing University of Science and Technology, Nanjing 210094, China
* Correspondence: hp@njust.edu.cn

Abstract: Taking advantage of the concurrent stretching and bending property of corrugated flexure hinges, a sinusoidal corrugated flexure linkage was proposed and applied for the construction of a corrugated dual-axial mechanism with structural symmetry and decoupled planar motion guidance. Castigliano's second theorem was employed to derive the complete compliance for a basic sinusoidal corrugated flexure unit, and matrix-based compliance modeling was then applied to find the stiffness of the sinusoidal corrugated flexure linkage and the corrugated dual-axial mechanism. Using established analytical models, the influence of structural parameters on the stiffness of both the corrugated flexure linkage and the dual-axial mechanism were investigated, with further verification by finite element analysis, with errors less than 20% compared to the analytical results for all cases. In addition, the stiffness of the corrugated flexure mechanism was practically tested, and its deviation between practical and analytical was around 7.4%. Further, the feasibility of the mechanism was demonstrated by successfully applying it for a magnetic planar nanopositioning stage, for which both open-loop and closed-loop performances were systematically examined. The stage has a stroke around 130 μm for the two axes and a maximum cross-talk less than 2.5%, and the natural frequency is around 590 Hz.

Keywords: dual-axial nanopositioning; corrugated flexure hinge; system modeling; trajectory tracking

Citation: Niu, Y.; Chen, X.; Chen, L.; Zhu, Z.; Huang, P. Development of a Sinusoidal Corrugated Dual-Axial Flexure Mechanism for Planar Nanopositioning. *Actuators* **2022**, *11*, 276. https://doi.org/10.3390/act11100276

Academic Editors: Jinchuan Zheng and Ioan Ursu

Received: 18 August 2022
Accepted: 27 September 2022
Published: 29 September 2022

1. Introduction

Flexure hinge-based planar XY nanopositioning stages in parallel are widely employed in the fields of micro-machining, micro-manipulation, and scanning-based surface metrology, to mention a few of the applications [1–3]. For state-of-the-art designs, dual-axial compliant mechanisms are symmetrically constructed by combining several flexure hinges having a single degree-of-freedom (DOF) of planar bending [4]. For example, four sets of "T"-shape mechanisms were employed in [4], for a total of 12 leaf-spring flexure hinges, and a combination of the bending motions of all the hinges jointly contributed to the decoupled dual-axial motions for the end-effector. Taking advantage of the right circular flexure hinges, a compound mechanism combining a separated prismatic joint and a parallelogram was developed to construct a decoupled XY nanopositioning stage in [5].

Although a structural configuration combining flexure hinges with the bending DOF dominates the current design of dual-axial nanopositioning stages, this increases structural complexity and the equivalent moving inertia caused by the employment of multiple flexure hinges [4,5]. To reduce structural complexity, simplified non-symmetric mechanisms having only two orthogonal parallelogram mechanisms were developed to guide the dual-axial motions, as reported in [6,7]. However, this simplified structure may lead to an unconstrained parasitic motion for the end-effector, which may greatly deteriorate the positioning accuracy of the planar stages. To overcome this defect, an alternative solution might be the adoption of flexure hinges to directly connect the end-effector and the base in a symmetric manner, which may simultaneously simplify the structure and guarantee accurate motion. In this condition, concurrent transition of planar bending and axial stretching deformations is essentially required for the flexure hinges to enable planar motions. As a candidate, "L"-shape flexure linkages are promising, and four sets of "L"-shape linkages may provide symmetric guidance for the motion along the two directions [8–10]. However, considering the corner structure of the linkage, it is difficult to arrange a parallel configuration for the multiple linkages to improve the resistance capability.

Recently, the concept of corrugated flexure hinges was developed and applied to construct dual-axial XY nanopositioning stages [11–13]. Along with a circular curve segment [14], a cone-shaped [15] segment was also developed to enrich the grouping of the corrugated flexural hinges. Following the conventional "T"-shape structure, corrugated hinges have also been applied to construct dual-axial XY nanopositioning stages [11–13]. As for those designs, the corrugated hinges were adopted to reduce the stress and extend the deformation range of conventional flexure hinges within a limited space [14], and the unique stretchable feature has not been explored for motion delivery. Since the "T"-shape structure was adopted for those designs, the resulting corrugated hinge-based planar stages may inevitably have similar defects as aforementioned.

To gain high-performance dual-axial guidance, we develop a dual-axial corrugated flexure mechanism with a simple structure and low moving mass. The main contributions of this study are: (a) A sinusoidal corrugated flexure hinge with a simple mathematical description is developed and comprehensively characterized by both analytical and finite element simulation methods. (b) The unique stretchable property is explored to realize concurrent stretching and bending of the corrugated flexure hinge for dual-axial motion guidance. (c) A corrugated dual-axial flexure mechanism is developed and demonstrated by applying it to a dual-axial electromagnetic stage.

The remainder of this paper is organized as follows: Section 2 introduces the sinusoidal corrugated hinge and derives its static compliance, Section 3 presents the developed corrugated dual-axial mechanism, and Section 4 demonstrates the parameter selection for constructing the dual-axial nanopositioning stage. The experimental testing of mechanism stiffness and the basic performance of the constructed dual-axial stage is detailed in Section 5, and the main conclusions are drawn in Section 6.

2. The Sinusoidal Corrugated Flexure Linkage

Although a sinusoidal corrugated beam was developed in [12] to clamp the movers to eliminate under-constraining, the complex stretching and bending property was not investigated for the corrugated beam. Herein, we introduce a monolithic sinusoidal corrugated flexure linkage, and the three-dimensional (3D) structure is illustrated in Figure 1. Along with the bending property, the linkage is intrinsically stretchable due to the structure corrugation, and multiple cycles may further enhance the flexibility for tuning the stretching stiffness.

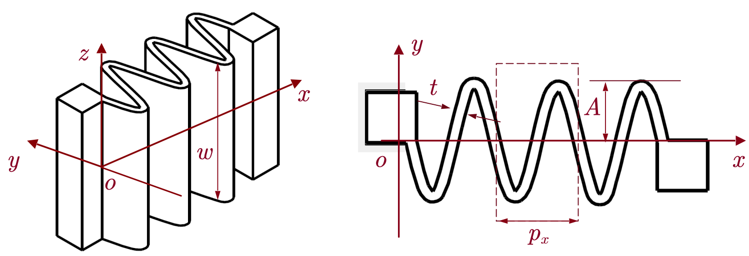

Figure 1. Structure of the sinusoidal corrugated flexure linkage with $n = 3$ for illustration.

Mathematically, the sinusoidal corrugated flexure linkage can be described by a simple and continuous equation as

$$z(x) = -A\sin(2\pi p_x^{-1} x),\ x \in [0, np_x] \tag{1}$$

where A, p_x, and n denote the amplitude, spatial periodicity, and cycle number of the linkage, respectively.

2.1. Stiffness Modeling of the Sinusoidal Corrugated Flexure Linkage

The sinusoidal corrugated linkage shown in Figure 1 can be decomposed into several (n) serially connected flexure units ($x \in [0, p_x]$). Assuming the load and corresponding deformation at the free end of the unit are, respectively, $\mathbf{F} = [f_x, f_y, f_z, m_x, m_y, m_z]^{\mathrm{T}}$ and $\mathbf{u} = [u_x, u_y, u_z, \theta_x, \theta_y, \theta_z]^{\mathrm{T}}$, the bending torques at position x can be expressed as

$$M_b(x) := \begin{cases} M_{xy}(x) = m_z + f_y(p_x - x) + f_x z(x) \\ M_{xz}(x) = m_y + f_z\sqrt{(p_x - x)^2 + z^2(x)} \\ M_{yz}(x) = m_x \end{cases} \tag{2}$$

and the planar normal and shear force are

$$\begin{cases} N(x) = f_y \sin\varphi + f_x \cos\varphi; \\ S(x) = -f_y \cos\varphi + f_x \sin\varphi \end{cases} \tag{3}$$

with

$$\varphi = \begin{cases} \arctan|\dot{z}|, \ x \in [\frac{1}{4}p_x, \frac{3}{4}p_x] \\ \pi - \arctan|\dot{z}|, \ \text{otherwise} \end{cases} \tag{4}$$

Therefore, following Castigliano's second theorem, the elastic strain energy can be expressed as [16]

$$\begin{aligned} U = & \int_0^{\mathcal{L}} \left(\frac{M_b^2(x)}{2EI} + \frac{N^2(x)}{2EA_c} + \frac{\alpha_s S^2(x)}{2GA_c} \right) \mathrm{d}s \\ = & \int_0^{p_x} \left(\frac{M_b^2(x)}{2EI} + \frac{N^2(x)}{2EA_c} + \frac{\alpha_s S^2(x)}{2GA_c} \right) \sqrt{1 + \dot{z}^2(x)}\mathrm{d}x \end{aligned} \tag{5}$$

where I is the second moment of the rectangular section of the corrugated beam, and $A_c = wt$ is the cross-sectional area. In addition, E represents the Young's modulus of the material, $G = \frac{E}{2(1+\mu)}$ is the shear modulus, with μ denoting the Passion's ratio, and $\alpha_s = \frac{12 + 11\mu}{10(1+\mu)}$ is the shear coefficient.

Accordingly, the spatial six-DOF compliance for the sinusoidal corrugated flexure unit can be obtained as [16,17]

$$\begin{cases} C_{x,f_x} = \dfrac{\partial^2 U}{\partial f_x^2}, \ C_{y,f_y} = \dfrac{\partial^2 U}{\partial f_y^2}, \ C_{z,f_z} = \dfrac{\partial^2 U}{\partial f_z^2}, \\ C_{\theta_x,m_x} = \dfrac{\partial^2 U}{\partial m_x^2}, \ C_{\theta_y,m_y} = \dfrac{\partial^2 U}{\partial m_y^2}, \ C_{\theta_z,m_z} = \dfrac{\partial^2 U}{\partial m_z^2}, \\ C_{\theta_z,f_y} = C_{y,m_z} = \dfrac{\partial^2 U}{\partial m_z \partial f_y}, \\ C_{\theta_y,f_z} = C_{z,m_y} = \dfrac{\partial^2 U}{\partial m_y \partial f_z}. \end{cases} \tag{6}$$

By substituting Equations (1)–(5) into Equation (6), the compliance items can be derived, which are presented in detail in Appendix A. Accordingly, the relationship between the deformations and loads for the flexure unit yields

$$\mathbf{u} = \mathbf{C}_s\mathbf{F} \tag{7}$$

where the compliance matrix $\mathbf{C}_s$ is defined as

$$\mathbf{C}_s = \begin{bmatrix} C_{x,f_x} & 0 & 0 & 0 & 0 & 0 \\ 0 & C_{y,f_y} & 0 & 0 & 0 & C_{y,m_z} \\ 0 & 0 & C_{z,f_z} & 0 & C_{z,m_y} & 0 \\ 0 & 0 & 0 & C_{\theta_x,m_x} & 0 & 0 \\ 0 & 0 & C_{\theta_y,f_z} & 0 & C_{\theta_y,m_y} & 0 \\ 0 & C_{\theta_z,f_y} & 0 & 0 & 0 & C_{\theta_z,m_z} \end{bmatrix} \quad (8)$$

Considering the serially connected flexure units (n) as shown in Figure 1, the complete compliance of the sinusoidal corrugated linkage can be derived following matrix-based compliance modeling (MCM) [18,19] as

$$\mathbf{C}_u = \sum_{i=1}^{n} \mathbf{T}_i \mathbf{C}_s \mathbf{T}_i^{\mathrm{T}} \quad (9)$$

where $\mathbf{T}_i$ is the compliance transformation matrix (CTM) to transfer the local coordinate system of the i-th flexure unit to the coordinate system of the linkage [18,19]. Accordingly, the stiffness matrix of the corrugated linkage can be derived as $\mathbf{K}_s = \mathbf{C}_s^{-1}$.

2.2. FEA-Based Stiffness Verification

FEA is conducted via commercial software ANSYS/Workbench to characterize the performance and to verify the stiffness model of the corrugated flexure linkage. Aluminum alloy (AL7075-T651) is selected as the material for the mechanism, with Young's modulus of $E = 72$ GPa and Poisson's ratio of $\mu = 0.33$. In addition, the adaptive meshing method provided by ANSYS/Workbench modulus is employed for element meshing. To guarantee simulation accuracy, the simulation was conducted using different scales of the element size, with the final scale chosen when further refinement did not lead to variation of the simulated results.

By setting the overall height $w = 8$ mm, there are four main parameters (A, t, p_x, and n) that can flexibly determine the deformation behavior of the flexure linkage. By fixing three of them, the stretchable (x-axis) and bending (y-axis) stiffness related to the one other parameter are obtained through both the analytical and FEA model, which are then comparatively illustrated in Figures 2 and 3, respectively. In general, the stretching stiffness is much higher than the bending stiffness, which may be attributed to the much larger equivalent bending length.

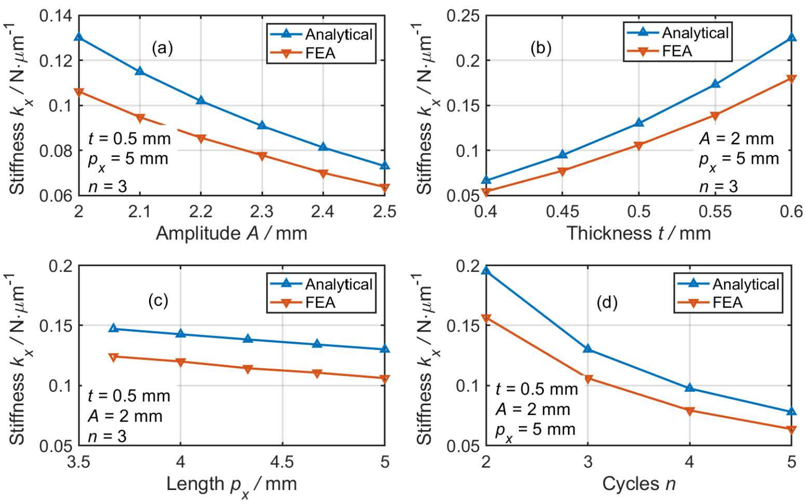

Figure 2. The x-axis stiffness k_x of the sinusoidal corrugated flexure hinge related to (**a**) amplitude A, (**b**) thickness t, (**c**) length p_x, and (**d**) cycle number n.

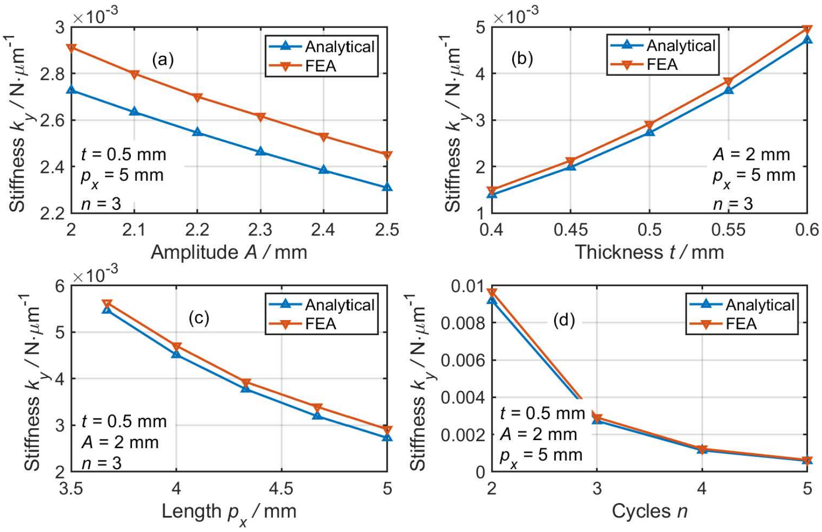

Figure 3. The y-axis stiffness k_y of the sinusoidal corrugated flexure hinge related to (**a**) amplitude A, (**b**) thickness t, (**c**) length p_x, and (**d**) cycle number n.

Although the stiffness values for the two directions are different for the linkage, their variation in relation to structural parameter changes are similar. As shown in Figures 2 and 3, an increase in amplitude A, unit length p_x, and cycle number n may decrease both the stretching and bending stiffness. By contrast, an exponential increase in stiffness may occur in terms of a linear increase in the thickness t. Overall, good agreement is observed between the analytical and FEA result, and all deviations between the analytical and FEA results for all cases are within 20%, verifying the effectiveness of the developed stiffness model for sinusoidal corrugated flexure hinges.

3. The Sinusoidal Corrugated Dual-Axial Mechanism

Taking advantage of the linkage, a sinusoidal corrugated dual-axial mechanism is constructed, as shown in Figure 4a. It mainly consists of four pairs of parallelograms arranged symmetrically, and each parallelogram has two parallel sinusoidal corrugated flexure linkages. For force balancing during axial elongation/compression, the two parallel linkages for each parallelogram are specially designed to have mirror-symmetry.

As illustrated in Figure 4b, when an actuation force (F_x for example) is applied, the double parallelograms along the actuation direction (x-axis) will stretch, and the other two double parallelograms (y-axis) will mainly bend to generate the x-axial motion with suppressed parasitic motions. Accordingly, dual-axial actuation forces on the end-effector may simultaneously generate axial stretching and planar bending for planar dual-axial motions.

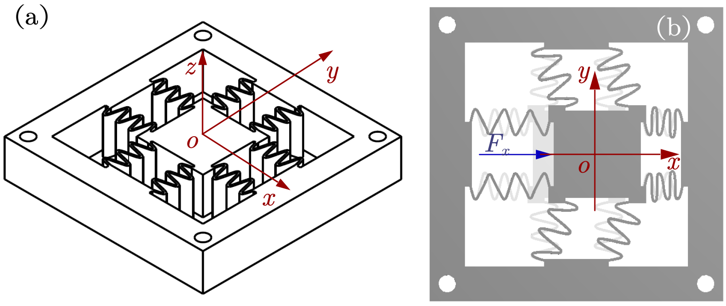

Figure 4. Structure of the sinusoidal corrugated dual-axial mechanism: (**a**) 3-D structure and (**b**) deformation principle.

3.1. Modeling of the Dual-Axial Mechanism

3.1.1. Stiffness Modeling

With respect to the k-th corrugated linkage, its compliance in the global coordinate system $o - xyz$ as shown in Figure 4 can be derived through MCM as

$$\mathbf{C}_L^{(k)} = \mathbf{T}_k \mathbf{C}_u \mathbf{T}_k^{\mathrm{T}} \tag{10}$$

where $\mathbf{T}_k$ is the CTM transferring the coordinate system of the k-th linkage to the global coordinate system of the mechanism.

Since the dual-axial mechanism is constructed by eight linkages in parallel, the stiffness for the mechanism can be derived as

$$\mathbf{K} = \sum_{k=1}^{8} \left(\mathbf{C}_L^{(k)}\right)^{-1} \tag{11}$$

Accordingly, x- and y-directional stiffness for the mechanism at point o is

$$k_x = k_y = \mathbf{K}(1,1) = \mathbf{K}(2,2) \tag{12}$$

3.1.2. Dynamics Modeling

Assume the generalized coordinate for the end-effector is $\mathbf{u} = [u_x, u_y]$. Following Lagrange's equation, by ignoring the damping effect, the dynamics equation for the mechanism can be expressed as

$$\mathbf{M}\ddot{\mathbf{u}} + \mathbf{K}\mathbf{u} = \mathbf{F} \tag{13}$$

where $\mathbf{M}$ represents the equivalent mass matrix, and $\mathbb{F}$ is the generalized force. In addition, the stiffness matrix for the mechanism is $\mathbf{K} = diag(k_x, k_y)$.

Considering the structural symmetry, the kinetic energy for the mechanism is

$$T = \frac{1}{2}\left(m\dot{u}_x^2 + m\dot{u}_y^2 + 4J\frac{\dot{u}_x^2}{l^2} + 4J\frac{\dot{u}_y^2}{l^2}\right) \tag{14}$$

where m is the equivalent moving mass, and J and $l = np_x$ are the rotational inertia and length of the corrugated hinge, respectively.

Accordingly, the mass matrix $\mathbf{M}$ yields

$$\mathbf{M} = \frac{\partial T}{\partial \dot{\mathbf{u}}}\dot{\mathbf{u}}^{-1} \tag{15}$$

and the resonant frequencies can be obtained through solving

$$\left|(2\pi f_i)^2\mathbf{M} - \mathbf{K}\right| = 0,\ i = x, y \tag{16}$$

3.2. FEA Verification of the Mechanism

Similarly, FEA-based simulation is further conducted using the same material and software for stiffness verification of the corrugated dual-axial flexure mechanism. As performed in Section 2.2, by fixing three of the four parameters, the directional stiffness k_x or k_y related to the selected parameter is presented in Figure 5. An increase in the amplitude A, unit length p_x, and cycle number n may lead to a decrease in the stiffness, whereas increasing the thickness t results in an increase in the stiffness. In addition, the maximum deviation between the analytical and FEA results is also smaller than 20% for all cases.

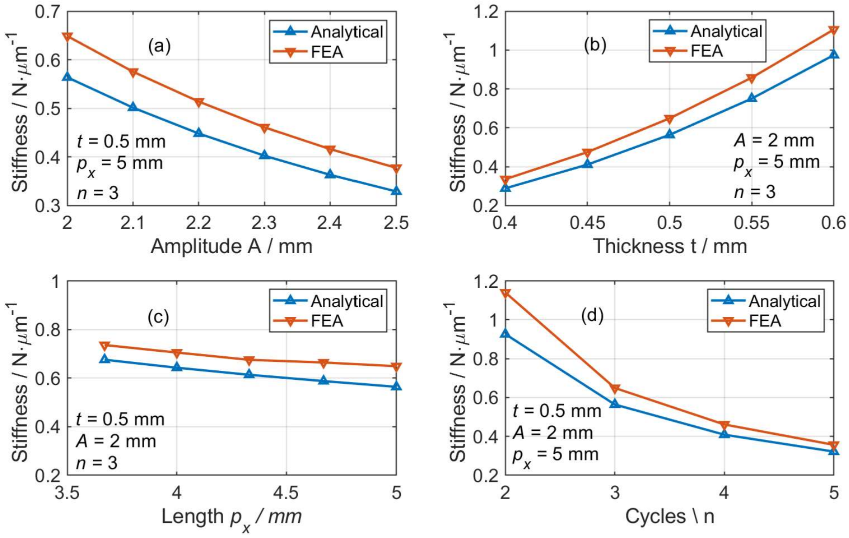

Figure 5. The stage's stiffness related to (**a**) amplitude A, (**b**) thickness t, (**c**) length p_x, and (**d**) cycle number n.

4. Structure Parameter Determination for a Planar Nanopositioning Stage

Since the mechanical structure is simple, the structure of the corrugated hinge may have a very limited influence on the equivalent moving mass. The working performance, including both the stroke and natural frequency, may highly depend on the stiffness of the mechanism. Therefore, only the axial stiffness is adopted as the design target for the construction of the planar nanopositioning stage, and it is set as $k_x = k_y = 0.4$ N/μm, taking into full consideration the actuation force.

Through trial-and-error, the dimensional parameters for the flexure linkages are determined as $A = 2.3$ mm, $t = 0.44$ mm, w = 9.4 mm, p_x = 3.33 mm, and $n = 3$, which lead to an analytical stiffness of 0.408 N/μm. By adopting the same FEA model as in Section 3.2, the directional deformation when subjected to an x-axial force of 100 N on the platform is illustrated in Figure 6a. Through dividing the driving force (100 N) by the deformation (199.76 μm), the stiffness is derived to be about 0.496 N/μm. Taking the FEA result as the benchmark, the analytical stiffness has an acceptable deviation around 20%. In addition, in-plane rotation is subjected to a torque (1 N·m) around the z-axis of the platform, which is illustrated in Figure 6b. The rotation angle of the platform is estimated to be about 0.0227 rad, which suggests an in-plane rotational stiffness of about 4.405×10^7 N·μm/rad. The analytical result is then found to have a deviation of about 19.4%.

As this paper mainly studies the flexible mechanism, only the moving part of the stage, including the flexible mechanism and the part directly connected to it, is considered in the dynamic simulation. By assembling all the necessary accessories for the planar stage demonstrated in Section 5.2, FEA simulation is employed to characterize the first four resonant modes of the dual-axial flexure mechanism, which are illustrated in Figure 7. As expected, the first two resonances have a nearly identical resonant frequency around 679 Hz, and the mode shapes are consistent with the desired dual-axial motions. Considering the structural symmetry, the analytical resonant frequencies for the first two resonant frequencies are calculated to be identical as 599.341 Hz, which deviates about 11.7% compared with the FEA result. In addition, out-of-plane translation and rotation are observed for the third and fourth mode, and the corresponding resonant frequencies are about 976.54 Hz and 1007.5 Hz, as shown in Figure 7c,d.

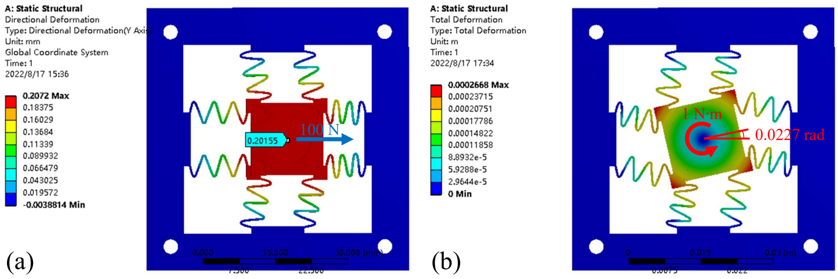

Figure 6. Simulated deformation of the platform: (**a**) axial deformation when subjected to an axial force of 100 N, and (**b**) rotation when subjected to a torque around the z-axis of 1 N·m.

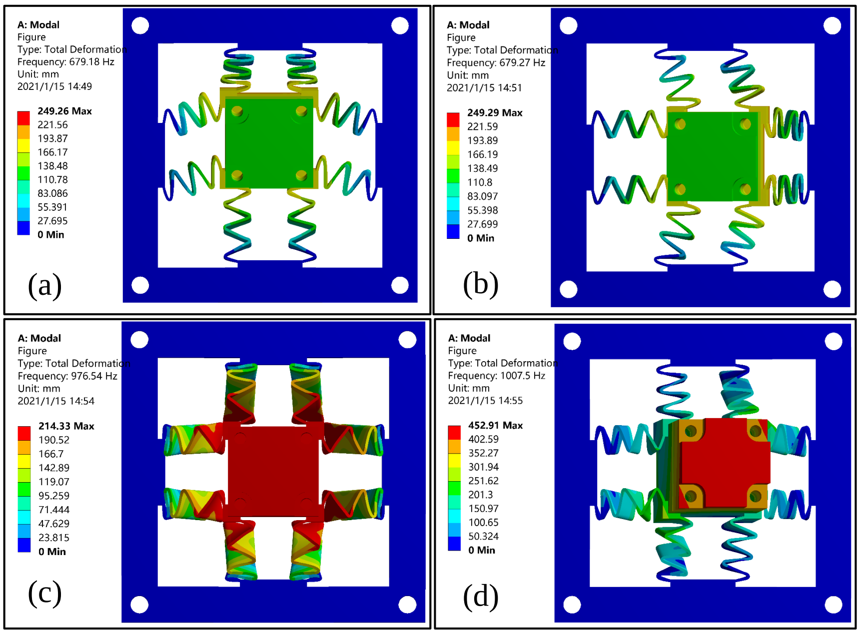

Figure 7. Simulated mode shapes: (**a**) first, (**b**) second, (**c**) third, and (**d**) fourth modes.

Note 1 The compliance and stiffness matrices of the designed stage are presented in Appendix A.3. From the calculated stiffness matrix **K**, the z-axial stiffness (10.8 N/μm) is about two orders of magnitude larger than the x- and y-axial stiffness (0.408 N/μm), suggesting that the out-of-plane DOF is well-constrained.

Note 2 Compared with the in-plane rotation, the much larger tilting stiffness around the x- and y-axes suggests that the two tilting DOFs are also constrained. Although the induced rotation is relatively small (1 N disturbance on the sidewall of the platform may only lead to a slight rotation of 0.17 mrad), undesired overly large in-plane torques must be carefully avoided to eliminate in-plane rotation errors for practical applications.

5. Experimental Results and Discussion

5.1. Stiffness-Testing the Mechanism

Using the selected structural parameters, the produced prototype of the sinusoidal corrugated dual-axial mechanism is shown in Figure 8a. The experimental setup in Figure 8b is developed for testing the stiffness of the mechanism. A force gauge with a digital display is employed to apply a directional force on the end-effector, and a dial indicator is used to record the resulting displacement.

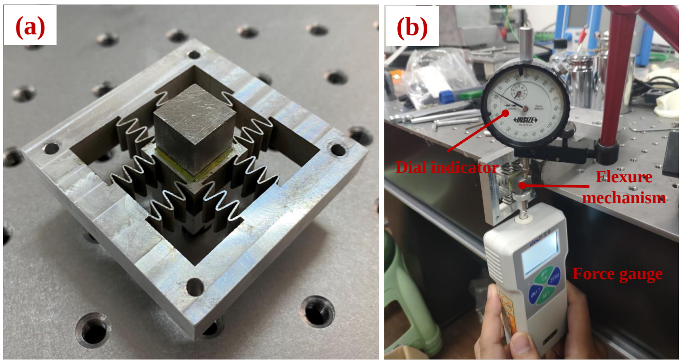

Figure 8. Photograph of (**a**) the mechanism prototype and (**b**) the experimental setup for stiffness measurement.

The obtained displacement related to the applied force for each direction is presented in Figure 9. From the best-fitted linear lines, the stiffness along the two directions is almost identical as $k_x \approx k_y = 0.38$ N/µm. Taking the practically tested stiffness as the benchmark, the analytical modeling error is about 7.4%.

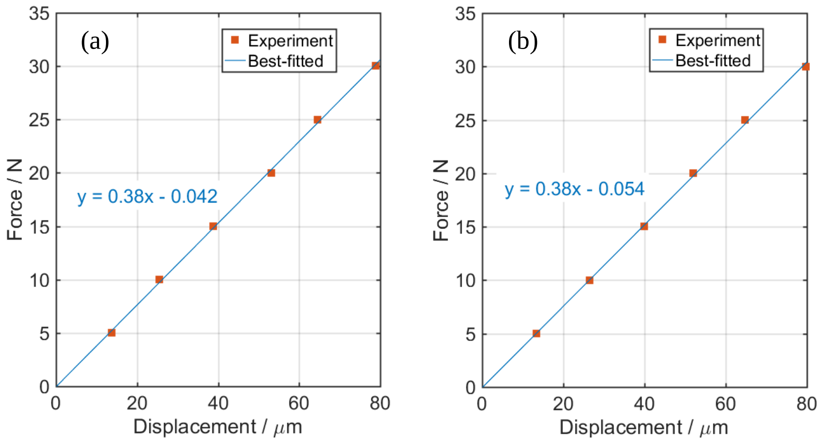

Figure 9. Relationship between applied force and resulting displacement for (**a**) the *x*-axis and (**b**) the *y*-axis.

5.2. Performance Testing for the Planar Stage

Practically, the feasibility of the sinusoidal corrugated dual-axial mechanism is demonstrated by applying it to a planar nanopositioning stage. With the stage, dual-axial normal-stressed electromagnetic forces are applied on the side surfaces of the armature, which is directly attached to the end-effector of the mechanism. Therefore, the actuation force is imposed on the end-effector and guides the corrugated mechanism during work. A detailed description of the newly developed electromagnetic actuator is presented in [20].

The photograph of the assembled planar nanopositioning stage is illustrated in Figure 10a, and the main components, including the electromagnetic and mechanical parts, are shown in Figure 10b. Two linear servo amplifiers (SMA5005-1, Glenteck Corporation, El Segundo, CA, USA) were adopted to amplify the command for driving the stage, and two ultra-precise capacitive sensors (Micro-sense-5810, Micro-sense Corporation, Lowell, MA, USA) were used to measure the end-effector motion. All the signals were collected and sent out through a data acquisition board (PCI-6259, NI Corporation, Austin, TX, USA) with a sampling frequency of 20 kHz.

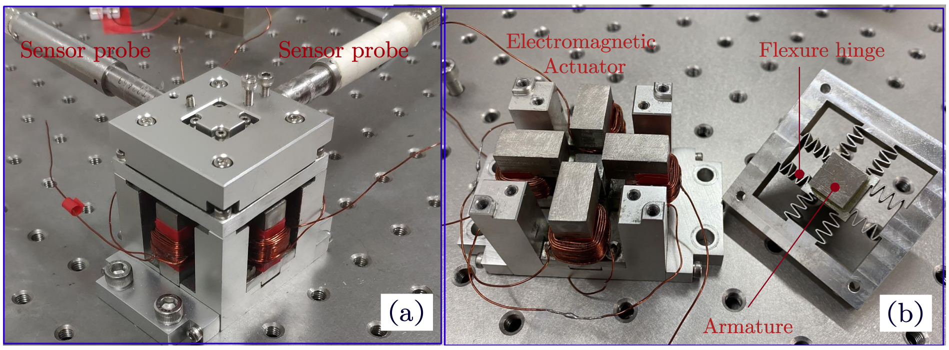

Figure 10. Photograph of the magnetic stage: (**a**) the assembled stage and (**b**) the key components.

5.2.1. Open-Loop Performance

A maximum allowable current of 3A was independently applied to the excitation coil winding for each direction, and the resulting primary motion and its cross-talk are shown in Figure 11. Overall, nearly identical strokes are observed: 133.5 µm and 132.6 µm for the *x*- and *y*-axis, respectively. The practical cross-talks are around 3.3 µm (2.47%) and 1.26 µm (0.95%), which might be caused by manufacturing errors in both the compliant mechanism and the electromagnetic actuator.

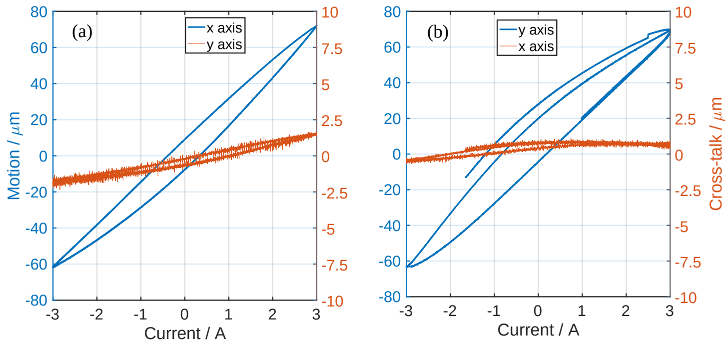

Figure 11. Motion and resulting cross-talk with maximum actuation along (**a**) the *x*-axis and (**b**) the *y*-axis.

In addition, taking advantage of the independent sweep excitation for each axis, the resulting frequency response functions for both axes are obtained and illustrated in Figure 12. As shown in Figure 12, the primary resonant frequencies for the two axes are identified as about $f_1 = 586$ Hz and $f_2 = 596$ Hz, and the smaller resonant peaks at $f_3 = 816$ Hz and $f_4 = 882$ Hz may correspond to the high-order resonances. Overall, the resonances exhibit good agreement with the simulation results obtained by FEA.

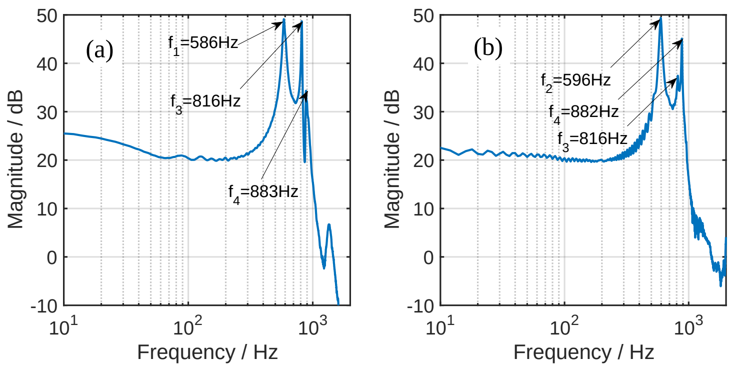

Figure 12. The amplitude response function of (**a**) the *x*-axis and (**b**) the *y*-axis.

5.2.2. Closed-Loop Performance

To perform trajectory tracking, a closed-loop system is constructed for the dual-axial nanopositioning stage. With the control system, each axis is treated as a single-input–single-output system (SISO), and the practical cross-talks and system hysteresis are lumped as the general disturbance to be compensated for by the feedback control [21].

The developed control system for each axis is schematically illustrated in Figure 13. The control system employs a typical proportional–integral–differential (PID) controller combining a system dynamics inversion-based feedforward compensator as the main controller for trajectory tracking [22,23]. Considering the lumped disturbance, a system model-based disturbance observer (DOB) is employed for disturbance compensation, as detailed in Figure 13. To simplify the controller design, the system nominal models for both axes are approximated by the system gains relating to the static input voltage and output motion, namely $P_m(s) \approx g_m$, and the PID parameters are tuned manually through trail-and-error.

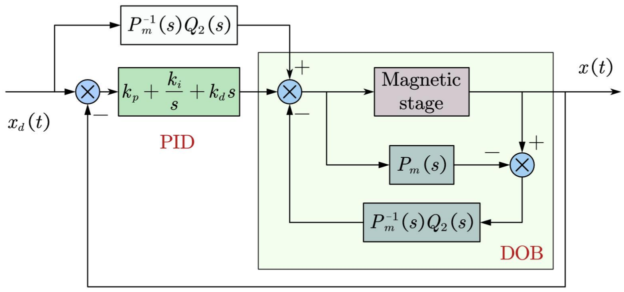

Figure 13. Schematic of the control loop, where k_p, k_i, and k_d are, respectively, the proportional, integral, and differential gains of the PID controller, and $Q_1(s)$ and $Q_2(s)$ are the low-pass filters.

The closed-loop performance of the stage is demonstrated by tracking a spiral trajectory. By setting $f = 30$ Hz as the motion frequency, the spiral trajectory can be mathematically expressed as

$$\begin{cases} x = 125t\sin(2\pi ft)\ \mu m \\ y = 125t\cos(2\pi ft)\ \mu m \end{cases} \tag{17}$$

The tracking result shown in Figure 14a suggests good accordance between the desired and practical motion. In addition, from the tracking error shown in Figure 14b,c, the maximum tracking error for both axes is observed to be less than ±0.5 µm, which is about ±1% of the full motion span.

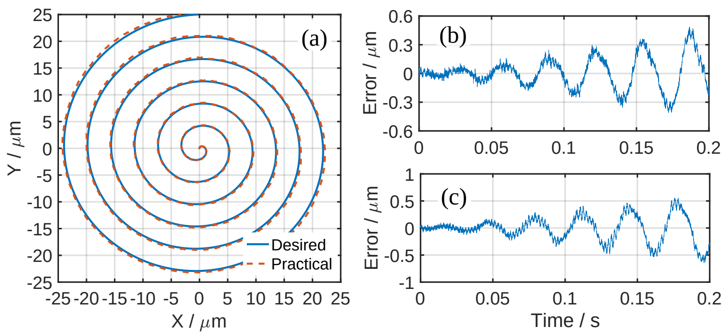

Figure 14. Trajectory tracking performance: (**a**) spiral trajectory tracking, and the error along (**b**) the *x*-axis and (**c**) the *y*-axis.

5.3. Results Comparison and Discussion

For comparison, the theoretical and practical performances including the stiffness and resonant frequency are summarized in Table 1. Considering the structure symmetry, only the stiffness k_x and the first resonant frequency f_x are presented, and the error between the analytical and practical results is also included.

Table 1. Performance comparison of the mechanism.

	k_x (N/μm)	f_x (Hz)
Analytical	0.408	599
FEA	0.496	679
Experiment	0.38	586
Error	7.4%	2.2%

As shown in Table 1, both the stiffness and natural frequency obtained by FEA are slightly larger than the analytical and experimental results, and better agreement is obtained between the theoretical and practical results. As for stiffness testing, the inevitable deformation of the clamped structure of the mechanism leads to overestimated motion when subjected to an external force. In addition, since the force is not consistent with the central axis of the end-effector, an extra torque is also imposed on the end-effector. The two factors may jointly lead to smaller practical stiffness.

In addition, the theoretical result only considers the mechanical structure, and the influence of the electromagnetic system on the final natural frequency of the stage is ignored. With the magnetic actuator, the actuation force is linearly related to the position of the armature, which may lead to a "negative" stiffness phenomenon for the nanopositioning stage [20,24]. Therefore, considering the "negative" stiffness effect, the natural frequency of the flexure mechanism might be slightly larger than the practically tested one presented in Table 1.

To illustrate the performance of the designed platform, comparisons with some typical dual-axial stages are presented in Table 2. As shown in Table 2, a much smaller size, a larger workspace, and a relatively high bandwidth are achieved in this work. Different from traditional designs, the proposed sinusoidal flexible hinge has two-degree-of-freedom planar bending, so it can realize a large range of two-axis motion in a limited volume. In addition, the designed mechanism does not have to consider complex input decoupling and driver protection issues due to the contactless electromagnetic actuation at the input ends, so high frequencies and large strokes can be achieved in a compact dimension. The coupling ratio of the designed mechanism is higher than that of the compared platforms. This may be due to the complex structure of the sinusoidal flexure hinge, which results in higher manufacturing errors than with the traditional design, and the assembly induced two-axis crosstalk at the input end.

Table 2. Performance comparison with state-of-the-art dual-axial stages.

Reference	Dimension (mm^2)	Workspace (μm^2)	Bandwidth (Hz)	Coupling Ratio (%)
[4]	165 × 145	31.5 × 31.5	570	0.7/0.9
[5]	142 × 142	40.2 × 42.9	483	0.58/0.56
[11]	-	1800 × 1820	72	-
[25]	160 × 160	55.4 × 53.2	253	0.42/0.45
[26]	190 × 190	19.5 × 19	2k	0.62/0.99
This work	54.4 × 54.4	133.5 × 132.6	586	2.47/0.95

6. Conclusions

A sinusoidal corrugated flexure linkage is proposed to concurrently stretch and bend, which is crucial to directly deliver dual-axial motions. Taking into full consideration this unique property, a corrugated flexure mechanism using four pairs of corrugated linkage-based parallelograms is developed for the planar nanopositioning stages to support and guide the dual-axial motions. The stiffness is analytically modeled for both the sinusoidal corrugated flexure linkage and dual-axial mechanism, and their deformation behavior related to the structural parameters are further investigated with finite element simulation-based verification. The deviation between the analytical and finite element result is less than 20% for all cases.

As for the dual-axial mechanism, the stiffness of the produced prototype is practically tested, and the deviation between the practical and analytical stiffness is around 7.4%. By applying the mechanism for the construction of a planar magnetic nanopositioning stage, a nearly identical stroke and resonant frequency are observed for the two axes, which are, respectively, around 130 μm and 590 Hz, and the maximum cross-talk is observed to be less than 2.5%. Finally, by adopting a PID-based main controller with the disturbance observer, the closed-loop performance of the dual-axis stage is also demonstrated.

Author Contributions: Conceptualization, Z.Z. and P.H.; methodology, Y.N.; software, Y.N. and X.C.; validation, Y.N., X.C. and L.C.; formal analysis, Y.N. and X.C.; investigation, Y.N. and X.C.; resources, Z.Z. and P.H.; data curation,Y.N. and X.C.; writing—original draft preparation, Y.N.; writing—review and editing, P.H. and Z.Z.; visualization, Y.N., X.C. and L.C.; supervision, Z.Z. and P.H.; project administration, Z.Z. and P.H.; funding acquisition, Z.Z. and P.H. All authors have read and agreed to the published version of the manuscript.

Funding: This research was funded by the National Natural Science Foundation of China(U2013211, 52275437, and 52105454), the Fundamental Research Funds for the Central Universities (30921013102), and the Guangdong Basic and Applied Basic Research Foundation (2020A1515111011).

Data Availability Statement: The data that support the findings of this study are available from the corresponding author upon reasonable request.

Conflicts of Interest: The authors declare no conflict of interest.

Appendix A

Appendix A.1. The Compliance Equations for the Sinusoidal Corrugated Flexure Unit

Let $\omega_x = \dfrac{2\pi}{p_x}$, $D_x = \sqrt{p_x^2 + 4A^2\pi^2}$, $E_1 = \text{EllipticF}\left(\omega_x x, \dfrac{4A^2\pi^2}{p_x^2 + 4A^2\pi^2}\right)$, and $E_2 = \text{EllipticE}\left(\omega_x x, \dfrac{4A^2\pi^2}{p_x^2 + 4A^2\pi^2}\right)$, for which EllipticF and EllipticE stand for the incomplete elliptic integral of the first and second kind, respectively. Accordingly, the detailed equation for the compliance term can be expressed as follows:

$$\begin{aligned} C_{x,f_x} =& \frac{\left(16A^4\pi^4 - p_x^4\right)E_2 + p_x^2 D_x^2 E_1}{2w\pi^3 t^3 E D_x} - \frac{A^2\sqrt{p_x^2 + 2A^2\pi^2 + 2A^2\pi^2\cos(2\omega_x x)}\sin(2\omega_x x)}{\pi w t^3 E} \\ &+ \frac{(12 + 11\mu)D_x^2 E_2 - (7 + 11\mu)p_x^2 E_1}{10\pi w t E D_x} \end{aligned} \tag{A1}$$

$$C_{y,f_y} = \frac{12\int_0^{p_x} (p_x - x)^2 \sqrt{1 + A^2(\omega_x)^2\cos^2(\omega_x x)}\,dx}{wt^3 E} + \frac{5D_x^2 E_2 - p_x^2(17 + 11\mu)E_1}{10\pi w t E D_x} \tag{A2}$$

$$C_{\theta_z,m_z} = \frac{6D_x E_2}{\pi w t^3 E} \tag{A3}$$

$$C_{\theta_z,f_y} = C_{y,m_z} = \frac{12\int_0^{p_x} (p_x - x)\sqrt{1 + A^2\omega_x^2\cos^2(\omega_x x)}\,dx}{wt^3 E} \tag{A4}$$

$$C_{z,f_z} = \frac{12\int_0^{p_x} \sqrt{1 + A^2\omega_x^2\cos^2(\omega_x x)}\left[(p_x - x)^2 + A^2\sin^2(\omega_x x)\right]dx}{tw^3 E} \tag{A5}$$

$$C_{\theta_y,m_y} = \frac{6D_x E_2}{\pi t w^3 E} \tag{A6}$$

$$C_{\theta_y,f_z} = C_{z,m_y} = \frac{12\int_0^{p_x} \sqrt{\left[1 + A^2\omega_x^2 \cos^2(\omega_x x)\right]\left[(p_x - x)^2 + A^2 \sin^2(\omega_x x)\right]}\, dx}{t w^3 E} \tag{A7}$$

$$C_{\theta_x,m_x} = \frac{12(1+\mu) D_x E_2}{\pi (t w^3 + w t^3) E} \tag{A8}$$

Appendix A.2. The Compliance Transformation Matrix

The compliance transformation matrix (CTM) is defined by [18,19]

$$\mathbf{T} = \begin{bmatrix} \mathbf{R}(\theta) & \mathbf{S}(\mathbf{r})\mathbf{R}(\theta) \\ \mathbf{O} & \mathbf{R}(\theta) \end{bmatrix} \tag{A9}$$

where $\mathbf{R}(\theta)$ is the required rotation operation for the local coordinate system to rotate to the global coordinate system in terms of a rotation angle of θ. For this study, the rotation is around the z-axis, which has the form of

$$\mathbf{R}(\theta) = \begin{bmatrix} \cos\phi & \sin\phi & 0 \\ -\sin\phi & \cos\phi & 0 \\ 0 & 0 & 1 \end{bmatrix} \tag{A10}$$

In Equation (A9), $\mathbf{S}(\mathbf{r})$ represents the position transformation, which is defined as

$$\mathbf{S} = \begin{bmatrix} 0 & -z_r & y_r \\ z_r & 0 & -x_r \\ -y_r & x_r & 0 \end{bmatrix} \tag{A11}$$

where $\mathbf{r} = [x_r, y_r, z_r]$ is the relative position of the local coordinate system in the global coordinate system.

Appendix A.3. The Characteristic Matrix of the Designed Stage

The compliance matrix for the sinusoidal corrugated flexure hinge designed for the mechanism is

$$\mathbf{C}_s = \begin{bmatrix} 4.02 & 0 & 0 & 0 & 0 & 0 \\ 0 & 7.88 & 0 & 0 & 0 & 0.0035 \\ 0 & 0 & 0.236 & 0 & 1.01 \times 10^{-5} & 0 \\ 0 & 0 & 0 & 1.21 \times 10^{-8} & 0 & 0 \\ 0 & 0 & 1.01 \times 10^{-5} & 0 & 4.57 \times 10^{-9} & 0 \\ 0 & 0.0035 & 0 & 0 & 0 & 2.09 \times 10^{-6} \end{bmatrix} \tag{A12}$$

The stiffness matrix for the sinusoidal corrugated dual-axial mechanism is

$$\mathbf{K} = \begin{bmatrix} 0.408 & 0 & 0 & 0 & 0 & 0 \\ 0 & 0.408 & 0 & 0 & 0 & 0 \\ 0 & 0 & 10.8 & 0 & 0 & 0 \\ 0 & 0 & 0 & 1.07 \times 10^{9} & 0 & 0 \\ 0 & 0 & 0 & 0 & 1.07 \times 10^{9} & 0 \\ 0 & 0 & 0 & 0 & 0 & 3.55 \times 10^{7} \end{bmatrix} \tag{A13}$$

References

1. Yong, Y.K.; Moheimani, S.O.R.; Kenton, B.J.; Leang, K.K. Invited Review Article: High-speed flexure-guided nanopositioning: Mechanical design and control issues. *Rev. Sci. Instruments* **2012**, *83*, 121101. [CrossRef] [PubMed]
2. Ortlepp, I.; Fröhlich, T.; Füßl, R.; Reger, J.; Schäffel, C.; Sinzinger, S.; Strehle, S.; Theska, R.; Zentner, L.; Zöllner, J.P.; et al. Tip-and Laser-based 3D Nanofabrication in Extended Macroscopic Working Areas. *Nanomanuf. Metrol.* **2021**, *4*, 132–148. [CrossRef]
3. Matsukuma, H.; Adachi, K.; Sugawara, T.; Shimizu, Y.; Gao, W.; Niwa, E.; Sasaki, Y. Closed-Loop Control of an XYZ Micro-Stage and Designing of Mechanical Structure for Reduction in Motion Errors. *Nanomanuf. Metrol.* **2021**, *4*, 53–66. [CrossRef]
4. Zhu, W.L.; Zhu, Z.; Guo, P.; Ju, B.F. A novel hybrid actuation mechanism based XY nanopositioning stage with totally decoupled kinematics. *Mech. Syst. Signal Process.* **2018**, *99*, 747–759. [CrossRef]
5. Wang, F.; Zhao, X.; Huo, Z.; Shi, B.; Liang, C.; Tian, Y.; Zhang, D. A 2-DOF nano-positioning scanner with novel compound decoupling-guiding mechanism. *Mech. Mach. Theory* **2021**, *155*, 104066. [CrossRef]
6. Zhu, Z.; Tong, Z.; To, S.; Jiang, X. Tuned diamond turning of micro-structured surfaces on brittle materials for the improvement of machining efficiency. *CIRP Ann.* **2019**, *68*, 559–562. [CrossRef]
7. Polit, S.; Dong, J. Development of a high-bandwidth XY nanopositioning stage for high-rate micro-/nanomanufacturing. *IEEE/ASME Trans. Mechatronics* **2010**, *16*, 724–733. [CrossRef]
8. Tian, Y.; Ma, Y.; Wang, F.; Lu, K.; Zhang, D. A novel XYZ micro/nano positioner with an amplifier based on L-shape levers and half-bridge structure. *Sens. Actuators A Phys.* **2020**, *302*, 111777. [CrossRef]
9. Zhu, Z.; To, S.; Ehmann, K.F.; Zhou, X. Design, analysis, and realization of a novel piezoelectrically actuated rotary spatial vibration system for micro-/nanomachining. *IEEE/ASME Trans. Mechatronics* **2017**, *22*, 1227–1237. [CrossRef]
10. Howell, L.L. Compliant mechanisms. In *21st Century Kinematics*; Springer: Berlin/Heidelberg, Germany, 2013; pp. 189–216.
11. Wang, N.; Zhang, Z.; Zhang, X.; Cui, C. Optimization of a 2-DOF micro-positioning stage using corrugated flexure units. *Mech. Mach. Theory* **2018**, *121*, 683–696. [CrossRef]
12. Xi, S.; Lai, L.J. Paired double parallelogram flexure mechanism clamped by corrugated beam for underconstraint elimination. *Rev. Sci. Instruments* **2020**, *91*, 086102. [CrossRef]
13. Li, C.; Wang, N.; Yue, F.; Zhang, X. Optimization of Translational Flexure Joints Using Corrugated Units Under Stress Constraints. *J. Mech. Robot.* **2021**, *13*, 061006. [CrossRef]
14. Wang, N.; Liang, X.; Zhang, X. Stiffness Analysis of Corrugated Flexure Beam Used in Compliant Mechanisms. *Chin. J. Mech. Eng.* **2015**, *28*, 776–784. [CrossRef]
15. Wang, N.; Zhang, Z.; Yue, F.; Zhang, X. Design and analysis of translational joints using corrugated flexural beams with conic curve segments. *Mech. Mach. Theory* **2019**, *132*, 223–235. [CrossRef]
16. Wu, J.; Zhang, Y.; Cai, S.; Cui, J. Modeling and analysis of conical-shaped notch flexure hinges based on NURBS. *Mech. Mach. Theory* **2018**, *128*, 560–568. [CrossRef]
17. Lobontiu, N.; Cullin, M. In-plane elastic response of two-segment circular-axis symmetric notch flexure hinges: The right circular design. *Precis. Eng.* **2013**, *37*, 542–555. [CrossRef]
18. Li, Y.; Xu, Q. Design and analysis of a totally decoupled flexure-based XY parallel micromanipulator. *IEEE Trans. Robot.* **2009**, *25*, 645–657.
19. Zhu, Z.; Zhou, X.; Liu, Z.; Wang, R.; Zhu, L. Development of a piezoelectrically actuated two-degree-of-freedom fast tool servo with decoupled motions for micro-/nanomachining. *Precis. Eng.* **2014**, *38*, 809–820. [CrossRef]
20. Zhu, Z.; Chen, L.; To, S. A novel direct drive electromagnetic XY nanopositioning stage. *CIRP Ann.* **2021**, *70*, 415–418. [CrossRef]
21. Khawwaf, J.; Zheng, J.; Chai, R.; Lu, R.; Man, Z. Adaptive Microtracking Control for an Underwater IPMC Actuator Using New Hyperplane-Based Sliding Mode. *IEEE/ASME Trans. Mechatronics* **2019**, *24*, 2108–2117. [CrossRef]
22. Yi, J.; Chang, S.; Shen, Y. Disturbance-observer-based hysteresis compensation for piezoelectric actuators. *IEEE/ASME Trans. Mechatronics* **2009**, *14*, 456–464.
23. Zhu, Z.; Chen, L.; Huang, P.; Schönemann, L.; Riemer, O.; Yao, J.; To, S.; Zhu, W.L. Design and control of a piezoelectrically actuated fast tool servo for diamond turning of microstructured surfaces. *IEEE Trans. Ind. Electron.* **2020**, *67*, 6688–6697. [CrossRef]
24. Ito, S.; Troppmair, S.; Lindner, B.; Cigarini, F.; Schitter, G. Long-range fast nanopositioner using nonlinearities of hybrid reluctance actuator for energy efficiency. *IEEE Trans. Ind. Electron.* **2018**, *66*, 3051–3059. [CrossRef]
25. Wang, F.; Huo, Z.; Liang, C.; Shi, B.; Tian, Y.; Zhao, X.; Zhang, D. A Novel Actuator-Internal Micro/Nano Positioning Stage with an Arch-Shape Bridge-Type Amplifier. *IEEE Trans. Ind. Electron.* **2019**, *66*, 9161–9172. [CrossRef]
26. Du, Y.; Li, T.; Jiang, Y.; Wang, H. Design and analysis of a 2-degree-of-freedom flexure-based micro-motion stage. *Adv. Mech. Eng.* **2016**, *8*, 168781401663830. [CrossRef]